DIVERTOR ARMOUR ISSUES: LIFETIME, SAFETY AND INFLUENCE ON ITER PERFORMANCE

S. Pestchanyi

Forschungszentrum Karlsruhe, IHM, P.B. 3640, D-76021, Karlsruhe, Germany

Comprehensive simulations of the ITER divertor armour vaporization and brittle destruction under ELMs of different sizes have revealed that the erosion rate of CFC armour is intolerable for an industrial reactor, but it can be considerably reduced by the armour fibre structure optimization. The ITER core contamination with carbon is tolerable for medium size ELMs, but large type I ELM can run the confinement into the disruption. Erosion of tungsten, an alternative armour material, under ELMs influence is satisfactory, but the danger of the core plasma contamination with tungsten is still not enough understood and potentially it could be very dangerous. Vaporization of tungsten, its cracking and dust production during ELMs are rather urgent issues to be investigated for proper choice of the divertor armour material for ITER. However, the erosion rate under action of the disruptive heat loads is tolerable for both armour materials assuming few hundred disruptions falls out during ITER lifetime.
PACS: 52.40.Hf, 52.55.Fa

1. INTRODUCTION

ELMy H-mode is the reference operational scenario foreseen for the future tokamak reactor ITER. Good confinement and a high thermonuclear plasma density associate in this mode with the edge localised modes (ELMs) of plasma instabilities. ELMs produce short periodic pulses of heat flux at the carbon fibre composite (CFC) divertor armour. During type I ELMs the heat flux rises on 2-3 orders of the magnitude over its stationary value.

The physical problems concerning the ITER discharge confinement, stability and thermonuclear plasma parameters are generally solved. But problems of the divertor armour lifetime and the core contamination with the armour material are still so grave that even the armour material choice has not yet been irrevocably done.

Simulations of armour erosion during the type I ELMs of a size, anticipated for ITER, have been performed in FZK using the FOREV-2D and the PEGASUS-3D codes, revealed that the CFC armour of 2 cm thickness will erode during few hundred ITER shots of 400 s duration. This is unacceptable for an industrial reactor. More of that, the type I ELMs produces carbon plasma, which contaminates the ITER core and decreases the thermonuclear gain of the reactor. Additional problems pose legislative restrictions on tritium inventory inside the ITER vessel. Tritium is mainly co-deposited in form of various hydrocarbons with carbon, eroded from the divertor armour. These problems have motivated investigations of alternative armour materials.

The only alternative divertor armour material could be tungsten. But last investigations of the tungsten behaviour under ELM-like heat loads have revealed severe cracking of the W armour tiles. Two more major drawbacks of W to be investigated are the dust production and possible severe contamination of the ITER core. Tungsten is extremely effective cooler for the thermonuclear plasma, so for allowable thermonuclear reaction gain its concentration in the core should be several orders of the magnitude lower than for carbon.

Investigation of the divertor armour erosion under influence of ELMs and disruptions as well as the ITER core plasma contamination with the eroded material are complicated problems, which can not be done in the modern tokamaks because ELMs there are too weak for the armour vaporization and brittle destruction. These problems are rather complicated for numeric simulations from the first principles. The only reasonable way for estimation of the anticipated divertor damage and ITER performance decrease is to use the available experimental facilities with plasma flux parameters closest possible for the ITER ELM and disruption ones for verification of codes and then, using the codes for extrapolations of the experimentally found results on ITER.

For these purposes the code FOREV-2D was developed, elaborated and tested during last fifteen years in FZK. The code is aimed on simulation of the divertor armour vaporization under influence of ITER transient events and modelling of transport of the contamination plasma in SOL, including diffusion of the plasma from SOL to the core and radiation cooling of the thermonuclear plasma.

The PEGASUS-3D code simulates cracking and dust production in fine grain graphites, CFCs of various grades and tungsten due to brittle destruction of the materials during severe surface heating with plasma fluxes characteristic for ITER transients. The simulation results has been validated using dedicated experiments in the MK-200UG plasma gun (TRINITI Troitsk, Russia) [1], QSPA-T (TRINITI) [2] and QSPA-Kh50 (IPP Kharkov, Ukraine) [3] plasma accelerators, JUDITH electron beam facility [4] (FZJ Julich, Germany) and GOL-3 facility [5] (Novosibirsk, Russia)

Description of the codes and their application to problems of ITER performance arising from the influence of ELMs and disruptions on the divertor are listed in this paper and modern understanding of their solutions is overviewed.

2. FOREV-2D

FOREV-2D is the magneto-hydrodynamics code with radiation heat transfer in magnetic flux coordinates. The code is designed for simulation of fast transient events, so it is assumed that the magnetic configuration remains unchanged during all the simulated process. The multifluid plasma is considered as a mixture of N compressible fluids, corresponding to all ion species of the pollutant, hydrogen isotopes and, possibly, helium.

The density of the k-th fluid is denoted as n_k, $0 \le k \le N$, $\mathbf{v}_k$ is the vector of k-th fluid velocity, T_k is the temperature of the k-th ion fluid, T_e and n_e are the electron temperature and density. These plasma parameters obey the multifluid hydrodynamics equations, described in details in [6]:

$$\frac{\partial n_k}{\partial t} + \nabla(n_k \mathbf{v}_k) = \left(I_+(n_{k-1}) + I_-(n_{k+1}) - I_+(n_k) - I_-(n_k)\right)$$

$$m_k n_k \left(\frac{\partial \mathbf{v}_k}{\partial t} + (\mathbf{v}_k \nabla)\mathbf{v}_k\right) + \nabla P_k + e z_k n_k \left(\mathbf{E} + \frac{1}{c}[\mathbf{v}_e \mathbf{B}]\right) = f_k$$

$$\nabla P_e + e n_e \left(\mathbf{E} + \frac{1}{c}[\mathbf{v}_e \mathbf{B}]\right) = f_e \qquad (1)$$

$$f_k = \sum_{l=0}^{N} \mathbf{F}_{kl} - \frac{z_k n_k}{n_e} \sum_{l=0}^{N} \mathbf{F}_{el} \qquad f_e = \sum_{l=0}^{N} \mathbf{F}_{el} - \frac{z_k n_k}{n_e} \sum_{l=0}^{N} \mathbf{F}_{el}$$

$$\frac{\partial E_k}{\partial t} + \nabla \mathbf{Q}_k = Q, \quad Q = \sum_{l=0}^{N} Q_{kl} + Q_{ke}$$

with m_k the mass of the k-th ion, $I_+(n_k)$ and $I_-(n_k)$ the ionisation and the recombination rates of the k-th fluid correspondingly, z_k the k-th ion charge, E_k the k-th fluid energy density, $\mathbf{Q}_k$ the vector of the k-th fluid energy flux, $P_k = n_k T_k$ the pressure of the k-th fluid, $\mathbf{F}_{kl}$ the friction force between the k-th and l-th fluid, $\mathbf{F}_{el}$ the friction force between the electrons and l-th fluid, Q_{kl} the energy exchange between k-th and l-th fluids, Q_{ke} the energy exchange between k-th fluid and electrons. The expressions for E_k and $\mathbf{Q}_k$ are given by

$$E_k = \tfrac{1}{2} m_k n_k \mathbf{v}_k^2 + E_k^{\text{int}},$$

$$\mathbf{Q}_k = P_k \mathbf{v}_k + m_k n_k \mathbf{v}_k \left(\tfrac{1}{2}\mathbf{v}_k^2 + E_k^{\text{int}}\right) + \mathbf{S}_k^{rad} \qquad (2)$$

with E_k^{int} the specific internal energy, $\mathbf{S}_k^{rad}$ the radiation heat flux from the k–th ions.

$$E^{\text{int}} = \frac{3}{2}\frac{p}{m_i} + E_{be} \qquad (3)$$

with $E_{be}(n, T_e)$ the ionisation and excitation specific energy of bound electrons.

The friction forces between the species a and b, including electrons are $\mathbf{F}_{ab} = \alpha_{ab}(\mathbf{V}_a - \mathbf{V}_b)$ with

$$\alpha_{ab} = n_a n_b m_{ab} \frac{4\sqrt{2\pi}\lambda z_a^2 z_b^2 e^4}{3\sqrt{m_{ab}}T^{3/2}}, \quad m_{ab} = \frac{m_a m_b}{m_a + m_b}, \quad e \text{ the}$$

proton charge and λ the Coulomb logarithm.

In order to achieve mathematical closure of the problem, Eqs. (1), (2) and (3) are supplemented with the equation for T_e that takes the form:

$$\tfrac{3}{2} n_e \left(\frac{\partial T_e}{\partial t} + \mathbf{v}\nabla T_e\right) + p_e \nabla \mathbf{v} = -\nabla \mathbf{q}_e + \sum_{k=0}^{N} Q_{ek} . \qquad (4)$$

The electron pressure $p_e = n_e T_e$, the velocity $\mathbf{v} = \sum_{k=0}^{N} m_k n_k V_k \Big/ \sum_{k=0}^{N} m_k n_k$. The electron thermal flux $\mathbf{q}_e$ and the ion-electron energy exchange term Q_{ek} are given by

$$\mathbf{q}_e = -\kappa_{e\|}\nabla_{\|} T_e, \quad Q_{ek} = 3\frac{m_e}{m_k}\frac{Z_k n_k}{\tau_e}(T_k - T_e) \qquad (5)$$

with m_e the electron mass, $\kappa_{e\|}$ the longitudinal thermal conductivity, τ_e the electron-ion collision time and $\nabla_{\|}$ the

operator of longitudinal gradient. The parameters τ_{ek} and $\kappa_{e\|}$ are given by

$$\tau_{ek} = \frac{3\sqrt{m_e}T_e^{3/2}}{4\sqrt{2\pi}\lambda e^4 Z_k^2 n_k}, \quad \kappa_{e\|} = A(Z)\frac{n_k T_e \tau_e}{m_e}. \qquad (6)$$

The function $A(Z)$ is equal

$$A(Z) = 12.5 - \frac{9.34}{1 + 0.223\max(0, Z-1)}. \qquad (7)$$

Multi-ray radiation transport (MRT) technique in toroidal geometry is used in FOREV-2D code for calculation of the radiation heat transport in carbon plasma. According to this approach radiation propagation along arbitrary straight line in any active medium, emitting and absorbing radiation, like in the tokamak plasma is adequately described by the Lambert-Beer-Bouguer law for radiation intensity I_n:

$$\frac{dI_n}{dl} = \beta_n - \kappa_n I_n, \qquad I_n(0) = 0 \qquad (8)$$
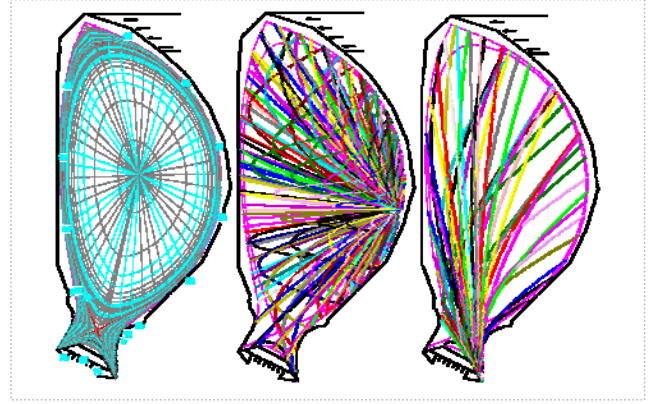

Fig. 1. FOREV-2D calculation grid (left) and two examples for the rays starting from the midplane of the outer wall (centre) and from the outer SSP (right)

The MRT approach for the radiation transport inside the active medium applied this low for the set of predefined radiation frequencies ω_n and for all possible ray directions crossing the active medium. Integration of the radiation intensity I_n is being carried out along the straight trajectories (the rays) traversing the spatial positions $\mathbf{r}$ in all directions of light propagation each of which is given by corresponding unit vector $\mathbf{n}$. In the poloidal section of tokamak the rays are the parabolas due to the toroidal symmetry as it is illustrated in Fig. 1. The rays propagate through the plasma with optical properties given by the emission- and absorption coefficients β_n and κ correspondingly. The trajectory equation is $\mathbf{r} = \mathbf{r}_0 + \mathbf{n}l$. The length l is the coordinate along the trajectory and $\mathbf{r}_0$ the original point chosen usually so that $I_n(\mathbf{r}_0) = 0$, thus assuming that the origins are situated close to the relatively cold first wall surface at which $\beta_n = 0$ is assumed. In this case $\mathbf{r}_0$ are parameterized by means of two independent surface parameters, which can be the toroidal- and the poloidal angles ζ and θ. The vector $\mathbf{n}$ gives two additional trajectory parameters (the azimuth- and polar angle of its direction) so that four independent real values are necessary to set one radiation ray. The rays propagate in two directions along each trajectory (the forward- and reverse ray). Thus, each starting element at

53

$\mathbf{r} = \mathbf{r}_0$ from which the forward rays start to propagate is in turn irradiated by the reverse rays which crossed the hot plasma with $\beta_n > 0$.

The radiation flux that crosses a face of the numerical cell is calculated as

$$q_r = 2 \int\limits_0^\pi d\varphi \int\limits_0^{\pi/2} I(\mathbf{n}) \sin \chi d\chi \qquad (9)$$

The toroidal symmetry allows reduction of integration on φ to the range 0-π. For numerical procedure the integration domain is subdivided into a several regions that have comparable contributions to q_r while $I_n(\mathbf{n})$ would be constant. Radiation intensity in each angle region is calculated as an average value over all the rays, crossing the face with the ray direction inside the region limits. The integration range in the azimuthal direction $0 \le \chi < \pi$ is subdivided on M equal regions of $d\chi = \pi/M$ size. In the polar direction $0 \le \varphi \le \pi$ sizes of the regions are equal for each of the M azimuthal slices and the number of regions in the polar direction $L(\chi)$ grows linearly from both poles to equator $d\varphi(\chi) = \pi/L(\chi)$.

3. PEGASUS-3D

A lattice model PEGASUS-3D has been developed and tested for numerical simulation of brittle destruction erosion of different CFC and fine grain graphite grades. For these simulations it is assumed that graphite consists of "crystalline" grains having different sizes and different anisotropy directions. Each graphite grain has some direction of axial symmetry of thermo-mechanical properties (the anisotropy axis). CFC consists of fibres with different properties along and across the fibre and of matrix, assumed to be fine grain graphite that fills the fibre interspaces. The term 'crystalline' denotes an imperfect crystal that can be treated as an object with some effective thermo-mechanical properties different from those of monocrystal. Fibres are a graphite material of cylindrical shape with the anisotropy axis along the fibre axis, so they can be treated as very large grains with anisotropic thermo-mechanical parameters. In PEGASUS the graphite materials are simulated using large 3D array of tightly packed cubic cells, so that the fibres and the grains of CFC consist of large number of cells having identical size a. A typical numerical lattice is shown in Fig. 2. The numerical sample is cut from a cubic array of up to 300x300x300 cubic cells. The origin of Cartesian coordinates situates at one of the cubic array vertices. The sample for the simulations is a slice, being 'cut' off the array by two planes perpendicular to the main diagonal, see Fig. 2. Such inclined orientation of the numerical sample is caused by necessity to eliminate the influence of cubic structure on the calculation results. The CFC matrix in the PEGASUS-3D code consists of grains with random shapes and sizes. The grain sizes have the Gaussian distribution. Additionally there are small grains filling the gaps between the larger ones or, alternatively, they may simulate pores. Neighbouring cells of the same grain (or fibre) are connected via internal bonds, cells of neighbouring grains via surface bonds.

The anisotropy of the physical properties of grains is determined by the atomic structure of graphite crystal. The thermal conductivity $\hat{\lambda}$ and the thermal expansion coefficient $\hat{\alpha}$ are the tensors of second rank with the eigenvalues λ_1 and α_1 along the anisotropy axis and the eigenvalue λ_2 and α_2 in two perpendicular directions. The Young's modulus $\hat{E}$ is a tensor of fourth rank and symmetry, corresponding to the hexagonal system [7]. Temperature dependences of the thermal conductivity, the density and the specific heat for 3 different directions (along and across the fibres) for NB31 CFC in temperature range 0…1000°C is known from [8,9]. Newest measurement of these parameters in temperature region 1000…2200°C has been done in [10]. Analysis of the last data has been done and conclusion that in the interval 1000…2200°C the thermal conductivity in pitch direction is inverse proportional to T [K] and for both perpendicular directions the conductivities are inverse proportional to square root of T [K] with accuracy of the data. It has been assumed that these dependences are valid at higher, most important for brittle destruction temperature region 2200…4000°C and used for the calculations. Besides, one should notice, that the data are for CFC sample, not for fibres and matrix. Nevertheless, using some reasonable assumptions one can extract the data on fibres and matrix from the measurements.
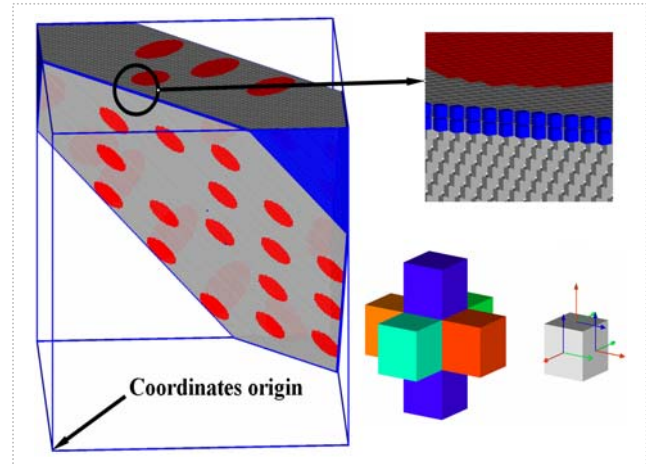

Fig. 2. Numeric CFC sample (left) produced from cubic array of cells for PEGASUS-3D simulations and the normal and two shear stresses acting on each cell face from neighbours (bottom right)

The strength of graphite crystalline is very different from the strength of the grains interfaces. To simulate the grain structure, we introduced two different parameters, the mean failure stress for the internal bonds σ_{0i} and the mean failure stress for the grain surface bonds σ_{0s}. The σ_{0i} and the σ_{0s} are dimensionless values normalised on the Young's modulus E_1 along the anisotropy axis. In case of broken bonds the expansion of the cells during the heating can result in a stretching (increasing distance between gap edges) or in compression (closure of gap edges with restoration of surface bonds). For the stretched gap the Young's modulus and the thermal conductivity of the bond are equal to zero. For a broken bond with compressed gap the Young's modulus of the bond is

assumed to be the same as for the unbroken bond and the thermal conductivity is reduced.

Calculation of CFC erosion using the PEGASUS-3D code starts from creation of the numerical sample that reproduces the required CFC structure and definition the heating conditions. Further simulation includes thermal transport, the thermostress calculation and cracking in the sample. Heated is the face of the sample closest to the origin. Similarity of the NB31 fibre structure and the numerical sample is seen in Fig. 3.
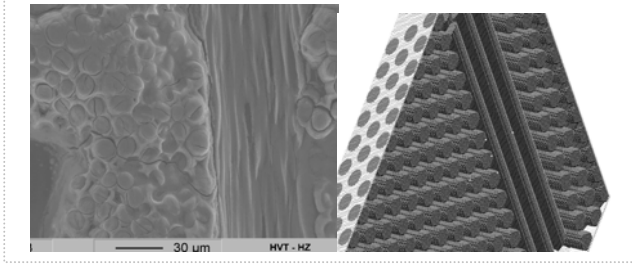

Fig. 3. Close view of the NB31 CFC surface (left) and its fibre structure simulated with PEGASUS-3D code (right). Matrix filling the interspaces between the fibres is not shown for clarity

Heating of a graphite sample results in thermostress due to anisotropic thermal expansion. In the model, the heating results in normal and tangential stresses acting on each bond of each cell. Using these stresses the displacements of the cells centres are calculated with ongoing temperature changes. Heated sample is at rest; therefore the sum of all forces acting on each cell should be equal zero. Mechanical stress equilibration is much faster than the propagation of the heat wave. Therefore it is assumed that after each change of temperature the mechanical equilibrium of the lattice establishes instantaneously.

In PEGASUS-3D the temperature distribution in the sample is described by the thermal conductivity equation

$$\frac{dT(\vec{r},t)}{dt} - \vec{\nabla}\hat{v}(\vec{r},T,t)\vec{\nabla}T(\vec{r},t) = \frac{Q(\vec{r},t)}{\rho c} \quad v_{ij} = \frac{\lambda_{ij}}{\rho c} \quad (10)$$

with T the temperature, ρ the density, c the specific heat, λ_{ij} the thermal conductivity tensor and $Q(\vec{r})$ the volumetric heating power. The elastic properties of the sample are described by a Born type Hamiltonian [11,12] which takes into account both normal and shear stresses

$$H = \sum_{i,j,k}\left(\frac{E_1}{2}u_{zz}^2 + 2E_1\left(u_{xx}+u_{yy}\right)^2 + 2E_3\left[\left(u_{xx}-u_{yy}\right)^2 + 4u_{xy}^2\right]\right.$$
$$\left. + 2E_4 u_{zz}\left(u_{xx}+u_{yy}\right) + 4E_5\left(u_{xz}^2 + u_{yz}^2\right)\right) \quad (11)$$

The sum is over all sample cells, E_1 - E_5 – five Young's modules of hexagonal crystal and u_{ij} – the deformation tensor of unhomogeneously heated sample, defined as:

$$u_{ij} = \frac{1}{2}\left(\frac{\partial u_i}{\partial x_j} - \frac{\partial u_j}{\partial x_i}\right) - u_{ij}^T . \quad (12)$$

The local deformation $u_{ij}^T = \frac{\alpha_{ij}}{3}(T - T_0)$ is due to the thermal expansion relative to the initial temperature T_0 and $u_i = (u_x, u_y, u_z)$ the cell centre displacement vector. Thermal expansion and mechanical interaction between the cells generates the thermostress σ_{ij}:

$$\sigma_{ij} = \frac{\partial H}{\partial u_{ij}} \quad (13)$$

Interaction of cells with the neighbouring ones and the stresses acting on the cell faces are illustrated in Fig. 2. The mechanical equilibrium of the system of interacting cells is calculated using a set of auxiliary dynamic equations

$$\frac{du_i}{dt} = \mathbf{F}_i = -\sum_j \frac{\partial H}{\partial u_{ji}} \quad (14)$$

The sum is over 6 i-th cell faces, $\mathbf{F}_i$ is the total force acting on the i-th cell. Eq. (14) is solved iteratively until the total force acting on each cell converges close to zero ($\mathbf{F}_i \approx 0$). Nevertheless, the stresses on the cell surfaces can remain rather large – of the order of $F \sim (\alpha_1 - \alpha_2)a^2 E_1(T - T_0)$ due to the anisotropy of grains. When the local stress exceeds the local failure strength value the bond cracks. To simulate the brittle destruction the following stress-failure criterion for each bond is used:

$$\sum_j |\sigma_{ij}| \geq \sigma_i^f . \quad (15)$$

The sum is over 3 stresses σ_{ix}, σ_{iy} and σ_{iz} of the same bond, σ_i^f the local failure stress value of the bond. It is assumed that σ_i^f is not the same for each bond; it defined as a random value with a distribution function to be determined by comparison with experiment. The characteristic mean value of the distribution function is designated as σ_{0s} and σ_{0i} for the surface and the internal bonds correspondingly. According to Eq.(15) the bond is assumed to be broken if the combination of normal and shear thermal stresses exceeds the value specified for this bond. This condition is checked after each time step and equilibration of mechanical stresses. The bonds for which it is fulfilled are disrupted.

A broken bond represents an elementary crack. The stress acting on the broken bond is automatically redistributed among the neighbour cells, increasing the probability for their failure. This process simulates the cracks propagation in the sample. Thus, the model takes into account that the mechanical properties of the sample depend on the crack density and are time-dependent. Merging of neighbouring cracks may produce a separate clusters of grains within the sample. Isolated clusters at the surface are removed as dust particles and the external heat flux is applied to the bulk surface, opened after the dust particle removal.

For the numerical simulation several samples with identical averaged properties, but with different realizations of random numbers defining the orientation of the grains and the failure stress values are generated. The numerical

procedure is repeated several times and the results (number of broken bonds, erosion rate) are averaged.

The PEGASUS-3D code has developed for simulations of the cracks in tungsten. For this simulation it has been assumed that the tungsten sample has no residual stress at initial temperature. Then, the surface heating of the sample was simulated simultaneously with the thermostress calculation. Heating of the sample leads to melting of a thin surface layer of a few micrometers thickness. The thermostress in the molten layer relaxed to zero and then, after stop of the surface heating the melt is resolidified. In the model developed, it was assumed that the resolidified layer is stress-less at the solidification temperature T_m. The calculations of PEGASUS-3D code continue further and simulate cooling down of the sample, compressive thermostress relaxation in the unmolten bulk and tensile thermostress generation in the resolidified layer. When the local thermostress value exceeds the local tensile strength value an elementary crack is produced. Stress concentration at the crack vertex and the crack propagation simulated self-consistently in PEGASUS-3D.

The fitting parameters of the model, the mean tensile strength for tungsten grains, σ_T^{gr} and for the grain boundaries, σ_T^{b} have been selected to reproduce the experimentally observed crack pattern. Calculations with the mean tensile strength for $\sigma_T^{b} = 0.5...1.5 GPa$ and $\sigma_T^{gr}/\sigma_T^{b} = 3$ has shown similar crack patterns with two different crack scales, the primary and the secondary ones. The characteristic primary crack mesh size increased with the σ_T^{b} value. The view on the simulated crack pattern and the cut of the sample irradiated in the QSPA-T facility are shown in Fig. 4.

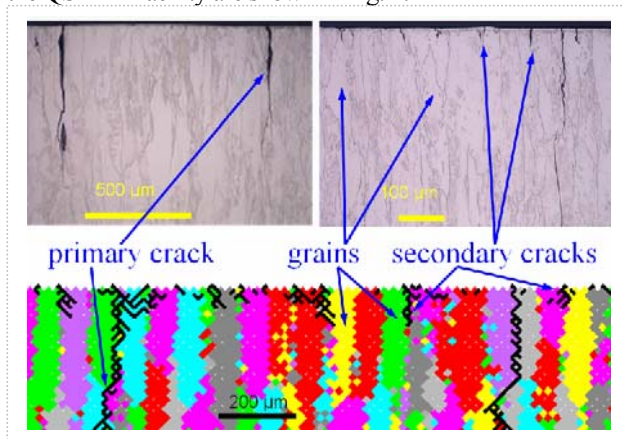*Fig.4. Comparison the tungsten sample irradiated in QSPA-T facility with the PEGASUS-3D simulation results. Shown are the grain patterns and the crack patterns in the cross section, perpendicular to the surface*

The primary cracks of the characteristic depth of ~500 μm and the mean distance between the cracks of 1...2 mm are seen in this panel. The upper right panel is the closer view of the sample cross section to illustrate the secondary cracks of ~50 μm mean depth and 100...200 μm average distance between the cracks. The lower panel is the cross section of the numerical sample after simulation of QSPA-T shot. The heating parameters correspond to the experimental ones. The fact that the simulations adequately reproduce the characteristic features of the cracks pattern proves that the physics of the cracking process was described appropriately.

56

CONCLUSIONS

Comprehensive simulations of the ITER divertor armour vaporization and brittle destruction under ELMs of different sizes have been performed. According to the results of the investigations, the erosion rate of CFC armour is approximately 1 μm per ITER ELM with energy deposition of ~1 MJ/m². This means that the armour survives few hundred ELMs only, which is intolerable for an industrial reactor. However, according to the PEGASUS-3D simulations [13] the erosion rate can be reduced at least by factor of five by optimization of the CFC fibre structure.

The ITER core contamination with carbon is tolerable for medium size ELMs, but large type I ELM can run the confinement into the disruption. From the simulations it follows that the carbon plasma production due to ELMs depends on the incoming heat flux increase rate $\dot{G}$. The dependences of erosion rate and total erosion on the heat flux increase rate are calculated. CFC armour erosion starts at $\dot{G} \approx 10G$ W/m²/ms, which corresponds to the local energy deposition of 0.8 MJ/m² per ELM, and saturates at ~ 6.5μm for ELMs with $\dot{G} \geq 200...350$ GW/m²/ms and the energy deposition of 10...15 MJ/m² per ELM.

After type I ELM, the carbon plasma having penetrated into the periphery of confinement region, re-radiates the electron thermal energy, decreasing the plasma temperature and the fusion power. Simulations of the tolerable ELM frequency as a function of ELM size are carried out using TOKES and FOREV-2D codes [14]. The FOREV-2D scenario has been proposed for simulation of the carbon plasma influx into ITER pedestal. Simulation of tolerable ELM frequency has been done for 3.5...12.1 MJ total ELM energies. The tolerable frequency is less than 10 Hz for the ELM of 7.3 MJ and decreases with increasing of the energy.

Simulations of ITER disruptions using the FOREV-2D code aiming on evaluation of radiation heat load at the first wall have been done. The erosion rate under action of the disruptive heat loads is tolerable for both armour materials assuming that few hundred disruptions falls out during ITER lifetime. An important peculiarity of the energy loss from the hot core during the thermal quench of the disruption has been revealed. According to the simulations, a considerable amount of carbon plasma vaporized from the divertor targets can penetrate into the core in the course of the disruption. This plasma can irradiate up to 85% of the thermonuclear plasma energy to the first wall, thus reducing the divertor heat load.

Experiments in the QSPA-T and QSPA-Kh50 facilities and the PEGASUS-3D simulations for ITER conditions have proved that the erosion of tungsten, an alternative armour material, under ELMs influence is of 0.06 μm/ELM. This erosion rate is satisfactory for ITER, but the influence of the core plasma contamination with tungsten plasma is still not enough understood and it potentially could be very dangerous. Especially dangerous is the vaporization of tungsten dust, produced due to the surface cracking under action of ELMs.

The results of experiments in the QSPA facility simulating the type I ITER ELM heat loads on the tungsten divertor tiles have shown an intense tungsten surface cracking. Analysis of the tungsten thermophysical parameters revealed its large potential for cracking: the thermostress due to thermal expansion from room temperature to the melting temperature

is more than one order of the magnitude larger then the tungsten tensile strength.

The code PEGASUS-3D has been updated for numerical simulation of tungsten surface cracking under the action of the thermostress arising in thin resolidified surface layer [15]. Numerical simulation of the experiments with melting of thin surface layer of tungsten resulted in qualitative agreement between the crack patterns. Both, experimentally observed and simulated crack grids consist of a coarse primary meshes formed of deep cracks and each coarse mesh is covered by shallower secondary crack grid with one order of the magnitude smaller depth.

An analytical model for cracks formation in tungsten under the tensile stress in the resolidified layer has been proposed. The model predicts development of cracks of several characteristic scales. It explains existence of the secondary fine grain crack grid by the thermostress relaxation due to the primary cracks in the resolidified layer. Cracking of tungsten under the compressive stress due to the temperature gradient without surface melting is the subject for further investigations.

Vaporization of tungsten, its cracking and dust production during ELMs are rather urgent issues to be investigated for proper choice of the divertor armour material for ITER.

REFERENCES

1. N. Arkhipov, V. Bakhtin et al. Erosion mechanism and erosion products in carbon-based materials // *Journal of Nuclear Materials*. 2002, v. 307-311, p. 1364-1368
2. A. Zhitlukhin, N. Klimov et al. Effects of ELMs on ITER divertor armour materials // *Journal of Nuclear Materials*. 2007, v. 363-365, p. 301-307
3. V.I. Tereshin, A.N. Bandura et. al. Application of powerful quasi-steady-state plasma accelerators for simulation of ITER transient heat loads on divertor surfaces // *Plasma Physics and Controlled Fusion*. 2007, v. 49, p. A231-A239.
4. R. Duwe, W. Kuehnlein et al // *Proc. 18th Symposium on Fusion Technology (SOFT), Karlsruhe Germany*. 1994, p. 355–358.
5. V.T. Astrelin, A.V. Burdakov et al. Hot electron target interaction experiments at the GOL-3 facility// *Nuclear Fusion*. 1997, v. 37, N 11, p. 1541-1558.
6. S.E. Pestchanyi, I.S. Landman, H. Wuerz Implementation of magnetic flux coordinates // RMHD code FOREV-2. Report of IHM 2002.
7. L.D. Landau, E.M. Lifshiz. *Course of theoretical physics. Theory of elasticity*. Oxford u.a.: "Butterworth-Heinemann". 1999, v. 7.
8. ITER MATERIAL PROPERTIES HANDBOOK.
9. J. P. Bonal and D. Moulinier. Thermal properties of advanced carbon fiber composites for fusion application. Rapport DMT/95-495, CEA. Direction des reacteurs nucleaires. Depertement de mecanique et de technologique. Oct. 1995.
10. Snecma propulsion solide. Departement developpement materiaux. Technical note. 15.10.2003. Reference FPTM 0393200A.
11. G.N. Hassold and D.J. Srolovitz // *Phys. Rev.* 1989, v. B39, 9273-9281.
12. J. Astrom, M. Kellomaki and J. Timonen // *Phys. Rev.* 1997, v. E55, 4757-4761.
13. S.E. Pestchanyi. Simulation of dust production in ITER transient events // *Fusion Engineering and Design*. 2008, v. 83, iss. 7-9, p.1054-1058.
14. S. Pestchanyi, I. Landman. ELM induced carbon contamination of ITER core // *Journal of Nuclear Materials*. 2007, v. 363–365, p. 1081–1086.
15. S.E. Pestchanyi, J. Linke. Simulation of cracks in tungsten under ITER specific transient heat loads // *Fusion Engineering and Design*. 2007, v. 82, iss. 15-24, p.1657-1663.

ПРОБЛЕМЫ ТЕПЛОЗАЩИТЫ ДИВЕРТОРА: ВРЕМЯ ЖИЗНИ, БЕЗОПАСНОСТЬ И ВЛИЯНИЕ НА ПРОИЗВОДИТЕЛЬНОСТЬ ИТЕРа

С.Е. Песчаный

Комплексное исследование процессов испарения и растрескивания теплозащиты дивертора под действием ELM в ИТЕРе выявило, что скорость эрозии теплозащиты из CFC неприемлемо велика для промышленного реактора, но она может быть значительно уменьшена при оптимизации стр企туры нитей CFC. Загрязнение ядра ИТЕРа углеродом некритично для ELMов средней энергии, но большой ELM типа I может вызвать срыв разряда. Скорость эрозии вольфрама, являющегося альтернативным материалом для теплозащиты, приемлемо мала, но опасность загрязнения разряда вольфрамом ещё недостаточно изучена, а потенциально это загрязнение очень опасно. Оценка испарения вольфрама, его растрескивания и пылеобразования во время ELM – это вопросы, требующие срочного решения для правильного выбора материала теплозащиты дивертора ИТЕРа. Однако эрозия обоих материалов под действием срывов вполне приемлема, если предположить, что в течение жизни ИТЕРа произойдёт несколько сот срывов.

ПРОБЛЕМИ ТЕПЛОЗАХИСТУ ДИВЕРТОРА: ТРИВАЛІСТЬ ЖИТТЯ, БЕЗПЕКА ТА ВПЛИВ НА ПРОДУКТИВНІСТЬ ІТЕРа

С.Є. Песчаний

Комплексне дослідження процесів випарування та розтріскування теплозахисту дивертора під впливом ELM в ІТЕРі виявило, що швидкість ерозії теплозахисту з CFC неприйнятно велика для промислового реактора, але вона може бути значно зменшена завдяки оптимізації структури ниток CFC. Забруднення ядра ІТЕРа вуглецем є некритичним для ELMів середньої енергії, але великий ELM типу I може призвести до зриву розряду. Швидкість ерозії вольфраму, який є альтернативним матеріалом для теплозахисту, прийнятно мала, але небезпека забруднення розряду вольфрамом ще недостатньо вивчена, а потенційно це забруднення дуже небезпечно. Оцінка випарування вольфраму, його розтріскування та пилоутворення під час ELM – це питання, які потребують термінового рішення для правильного вибору матеріалу теплозахисту дивертора ІТЕРа. Однак ерозія обох матеріалів під впливом зривів цілком прийнятна, якщо припустити, що під час життя ІТЕРа відбудеться декілька сотень зривів.